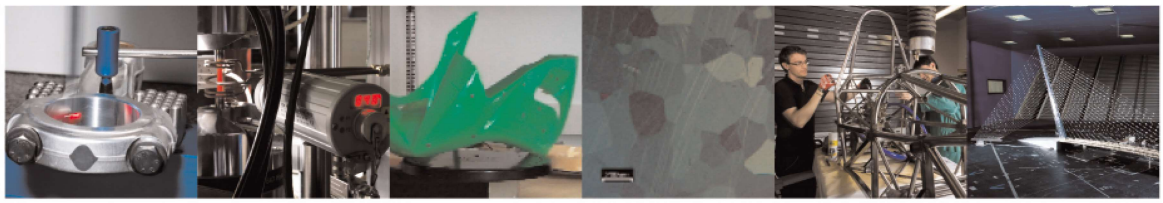

Effect of printing parameters on mechanical properties of extrusion-based additively manufactured ceramic parts

Rane, K.; Farid, M. A.; Hassan, W.; Strano, M.

DIPARTIMENTO DI MECCANICA ■ POLITECNICO DI MILANO
via G. La Masa, 1 ■ 20156 Milano ■ EMAIL (PEC): pecmecc@cert.polimi.it
http://www.mecc.polimi.it
Rev. 0

Effect of printing parameters on mechanical properties of extrusion-based additively manufactured ceramic parts

Kedarnath Rane*, Muhammad Asad Farid, Waqar Hassan, Matteo Strano

Dipartimento di Meccanica, Politecnico di Milano, Via La Masa 1, Milan, Italy

**Corresponding author. Tel: +39-0223998534, E-mail: kedarnath.rane@polimi.it*

Abstract

The purpose of this study is to investigate the effect of printing parameters on the physical and mechanical properties of additively manufactured ceramics (alumina and zirconia). Sample parts were obtained by extrusion-based additive manufacturing of a ceramic-binder mixture and subsequent post-processing (debinding and sintering). Their mechanical properties (microhardness, flexural strength, toughness) were measured and correlated with the printing parameters. Part orientation is the most significant factor for microhardness and flexural strength in both ceramic materials. Parts with vertical orientation show higher hardness while horizontal samples show higher flexural strength compared to their respective counterparts. Extrusion velocity was found to be insignificant for hardness and flexural strength. However, a marginal increase in fracture toughness with the increase in the extrusion velocity was observed. The fracture toughness of additively manufactured ceramics shows an increasing trend with elastic modulus and flexural strength and a decreasing trend with hardness and sintered density.

Keywords: alumina; zirconia; printing parameters; sintering; fracture toughness

1. Introduction

Engineering ceramics have numerous useful properties, such as high hardness, stiffness, strength retention at elevated temperatures, corrosion resistance associated with chemical inertness, etc. Moreover, they have about 50 % lower density than steel, which makes them suitable for technical applications where high strength and high temperature stability are the key functional requirements [1]. Alumina is known because of its excellent mechanical and thermal properties at elevated temperature. Zirconia is another common ceramic material, today used for several applications such as body-implants, dental crowns, oxygen sensors and several microcomponents. It shows

high toughness, thermal insulation, biocompatibility [2], and ionic conductivity [3]. The combination of high transparency, large refractive index, and high dielectric constant makes this ceramic material interesting for optical applications. The addition of yttrium oxide greatly increases the electrical and mechanical properties of Zirconia. A unique combination of mechanical and optical properties can be achieved by polycrystalline cubic Zirconia with 8 mol% of Y_2O_3 [4].

1.1 Hardness and flexural strength of alumina and zirconia

Hardness and flexural strength are the most important properties of alumina and zirconia, and they deserve a deeper investigation of the scientific literature. Several efforts have been made to predict the hardness and fracture toughness of alumina using different alumina compositions, different manufacturing technologies, and different procedures to calculate the hardness of alumina. Anstis et al. employed a simplified two-dimensional fracture mechanics analysis [5]. Apholt and colleagues determined the flexural strength of dental alumina and zirconia using the three-point bending test [6]. The static and dynamic flexural strength of 99.5 % alumina were compared in [7] The flexural strength of alumina, out of the literature review, can be assessed in the range between 260 and to 360 MPa.

Ćorić et al. analyzed the fracture toughness of yttria-stabilized tetragonal zirconia (Y-TZP) dental ceramics by the Vickers indentation fracture test (VIF) [8]. The average Vickers hardness should be around 1337 HV. The hardness of Zirconia depends on its relative density and on the addition of dopants [9]. An increase of relative density from 95% to 98 % makes the hardness almost more than double. Zirconia stabilized by small percentages of Yttria increases its hardness significantly.

1.2 Additive manufacturing of technical ceramics.

The use of Additive Manufacturing (AM) for ceramics will expectedly raise with the continuous improvement of the technology [10], especially for slurry based processes [11] and selective laser sintering (SLS) [12]. Although AM processes allow to realize relatively complex geometries [13], their advantage is significantly compromised by the lack of microstructural quality control within the ceramic parts [14]. Often, efforts to additively manufacture ceramic components result in parts with defects (i.e., flaws or large porosity as a result of the AM process). Various other issues such as purity, dimensional accuracy, surface quality, and interfacial defects commonly exist with AM

ceramic structures. Furthermore, due to the staircase effect, inherent to AM processes, the notch sensitivity of the printed ceramic parts is also relevant [15].

Slurry based processes are similar to EAM, since they deposit an aqueous viscous suspension (e.g. ~50 vol% solid loading) of ceramic powder in a layer-by-layer fashion [16]. Liu and Huang manufactured Al_2O_3 complex ceramic products by using SLS. After debinding and sintering processes, final Al_2O_3 ceramic bodies could have a relative density of 93% [17]. The Selective Laser Melting (SLM) processes for of ceramic powder was described for zirconia-alumina ceramic components [18], able to achieve almost 100 percent relative density, with no post-processing, producing specimens with more than 500 MPa flexural strength. Remaining challenges are the stresses caused by the deposition of the cold powder layers on top of the preheated ceramic, and the rough surface quality. Polzin et al. demonstrated the feasibility to manufacture complex porous ceramic parts with a 3D direct ink printing; however, the Al_2O_3 parts were highly porous with 69.27% [19]. Defect-free alumina parts have also been fabricated by Liu, which combined the stereolitography (SLA) process with water debinding. These properties of Al_2O_3 parts were like those prepared by the conventional shaping method. SLA has been frequently used to produce useful parts such as casting moulds and cores [20] or cutting tools [21].

Extrusion based Additive Manufacturing (EAM) is aimed at producing components with a high build up rate and at a lower cost per part, compared to other additive manufacturing techniques. One of the key advantages of this process is its versatility and ability to additively manufacture a range of materials, including metals, composites and ceramics [22] [23]. There is no industrialized or mainstream ceramic product manufactured with EAM processes. Nonetheless, the literature referring to shape stability during printing and sintering is continuously growing and soon the process will find its applicability in industries.

The EAM process involves four stages: feedstock preparation, 3D printing, debinding and sintering. The used feedstock is a homogeneous mixture of metal/ceramic powder and binders. 3D printing is accomplished by synchronizing the extrusion of the feedstock material with moving table or extrusion head. There are three possible feeding systems: a pinch feed mechanism adopts spooled filament of a feedstock, whereas syringe/piston-based and screw-based extrusion system need pelletized feedstock for 3D printing [23]. The part obtained after 3D printing is called “green”. During the subsequent stages the green part undergoes significant modifications: during

debinding, the removal of binder constituents takes place; in sintering, powder particles get consolidated to near full density. As the part undergoes treatment at these stages, the final characteristics of the part is dependent on multiple parameters.

Ceramic powder Injection Molding (CIM) can be identified as the enabling technology for EAM. Therefore, a wide literature is already available relating to effect of feedstock material, debinding and sintering parameters on final characteristics [24]. However, the printing parameters which are alike to Fused Deposition Modeling are expected to act differently because of the interaction with subsequent debinding and sintering stages.

According to the literature, the most influential parameters are shown in Figure 1 and comprise of material parameters (powder and binder properties) and process parameters of the 3D printing, debinding and sintering stages [25]. Despite some recent papers are available that describe the AM process for alumina and zirconia by extrusion of highly filled polymers [26], there is no study that correlates the 3D printing process parameters to the mechanical properties. The present work is an attempt to fill this gap and investigates experimentally the effect of part orientation and extrusion velocity on the physical and mechanical properties of 3D printed parts by EAM process.

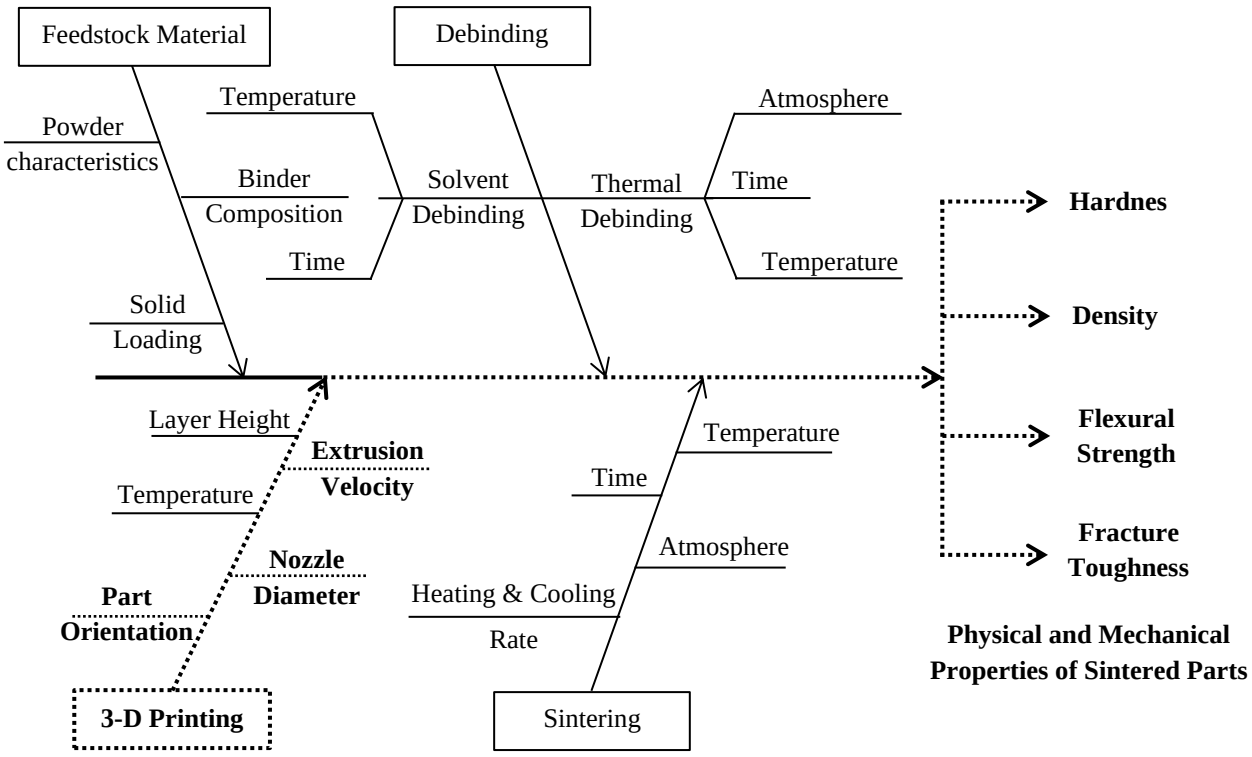

Figure 1: Ishikawa Diagram of process parameters and properties of sintered EAM parts

2. Materials and methods

2.1. Materials

In this study, two feedstocks having powder loading of ceramics were considered. Commercially available feedstock in pelletized form (K1008 and K1009 by Inmafeed) were procured for alumina (Al_2O_3) and zirconia (ZrO_2) respectively. Theoretical density of Al_2O_3 is 3.95 g/cm³ and ZrO_2 is 6.1 g/cm³ respectively. The median particle size (d_{50}) for Al_2O_3 is 2 µm and ZrO_2 is 0.6 µm respectively. The chemical composition of the used ceramic powders is provided in Table 1. Powder was composed majorly of Al_2O_3 particles for alumina feedstock. In the zirconia feedstock the ZrO_2 powder is stabilized with 5.15 wt.% Y_2O_3 (YSZ).

Table 1: Chemical composition of ceramic powder used in the present study

Alumina	Na_2O	MgO	CaO	Fe_2O_3	SiO_2	Al_2O_3
Wt.%	0.1%	0.9%	1.3%	0.03%	1.8%	96%
Zirconia	Y_2O_3	Al_2O_3	SiO_2	Fe_2O_3	NaO_2	ZrO_2
Wt.%	5.15%	0.25%	0.02%	0.01%	0.04%	94.5%

Powder loading used for these feedstocks was also different, for alumina it was 60 vol.% and for zirconia it was 47 vol.%. The binder constituents were not revealed by supplier but according to the specifications, the major volume of (sacrificial) binder is water soluble and the remaining polymeric binder can be removed during thermal debinding step. The shear viscosity of the two feedstocks has been characterized by means of a twin barrel capillary rheometer. The shear viscosity (η_s) can be modelled with a power-law equation as a function of the corrected shear strain, once fixed the proper extrusion melt temperature:

$$\eta_s = K\,\dot{\gamma}^{n-1} \quad \ldots\ldots\ldots\ldots\ldots\ldots\ldots\ldots (1)$$

The elongational viscosity η_E, which is dominant in EAM processes with respect to shear viscosity [27], can be modelled with a similar equation:

$$\eta_E = l\dot{\gamma}_a^{y-1} \quad \ldots\ldots\ldots\ldots\ldots\ldots\ldots\ldots (2)$$

The main properties of the feedstocks, including the rheological parameters *K*, *l*, *y* and *n*, are summarized in Table 2. The main differences are that the zirconia feedstock has a much larger heat capacity C_p and a much larger elongational consistency *l*.

Table 2: Physical and thermal properties of feedstock used in the present study; d_{50} is the mean diameter of the powder, φ is the powder loading (vol%) in the feedstock, and ρ, k, and Cp are the density, thermal conductivity, and heat capacity of the feedstock, respectively. The thermally sensitive parameters are calculated at 145 °C for alumina and 170°C for zirconia.

Feedstock	d_{50} (μm)	φ (vol.%)	ρ (kg/m^3)	k (W/m K)	C_p (J/kg K)	α (vol.%)	K (Pa.s)	n	L (kPa.s)	y
Al_2O_3-binder	1.9	60	2.40	0.63	1.53	0.17	5.22	0.28	1.09	0.21
ZrO_2-binder	0.6	47	2.55	0.43	794	0.21	3.62	0.59	6.57	0.05

2.2. 3D printing of ceramic feedstock

The ceramic feedstocks described in Section 2.1 were used for producing test parts using Extrusion based Additive Manufacturing (EAM) process. A specially designed EFeSTO (Extrusion of Feedstock for the manufacturing of Sintered Tiny Objects) machine was employed for 3D printing of ceramic feedstock. The machine is equipped with a powerful extrusion unit, which allows controlled deposition of molten feedstock at low shear rates (10 to 250 s^{-1}). The extrusion takes place onto a movable platform, with reverse delta mechanism kinematics.

The feedstocks were 3D printed by using two different nozzles, *Dn*=0.4 mm for alumina and *Dn*=0.8 mm for zirconia. This is because zirconia feedstock showed inferior extrudability based on preliminary experiments carried out to test rheological characteristics of feedstock [27]. With increased *Dn*, deposition of zirconia improved with a marginal loss on surface quality. Two different shapes were considered: cylindrical shapes with a base diameter of 10 mm and a height of 10 mm; bars having a rectangular cross section with 6 mm height, 60 mm length and 10 mm width. The rectangular bar was printed in a "horizontal" orientation, laying on the face of dimensions 60 X 10 mm, and a "vertical" orientation, laying on the 60 X 10 mm face, to experiment different layer orientations. For alumina feedstock, a total of 27 parts were printed using a nozzle of diameter (*Dn*) of 0.4 mm, layer height (*h*) of 0.2 mm, extrusion temperature (*Te*) of 145°C and three different extrusion velocities (*Ve*), as shown in Figure 2. Similarly, zirconia parts were 3D printed by employing the same experimental plan, but with *Dn* of 0.8 mm, layer height (*h*) of 0.4 mm, and extrusion temperature (*Te*) of 175°C. As the aim of present study is to determine mechanical strength of 3D printed ceramic parts, the outer contour profile which is responsible for surface quality of the parts is discarded and rectilinear infill path with fill angle 45^o

as shown in Figure 3 (a) is considered. Open source *Slic3r* software is used for generating g-codes for each part. The deposition of material is programmed through these g-codes for each layer as shown in Figure 3 (b) and (c) wherein the difference between rectilinear paths generated for first and second layer is presented. It should be noted that due to different printing setting of alumina (*Dn*=0.4 mm, *h*= 0.2 mm) and zirconia (*Dn*=0.8 mm, *h*= 0.4 mm), the number of layers and thereby printing time is almost halved for zirconia parts with reference to alumina parts. As an example, for printing of horizontal rectangular bar shaped part (dimensions 60 mm x 10 mm x 6 mm) at *Ve* = 7.5 mm/s, it requires 84 minutes (30 layers) to print one alumina part whereas one zirconia part only needs 15 layers and about 28 minutes of printing time.

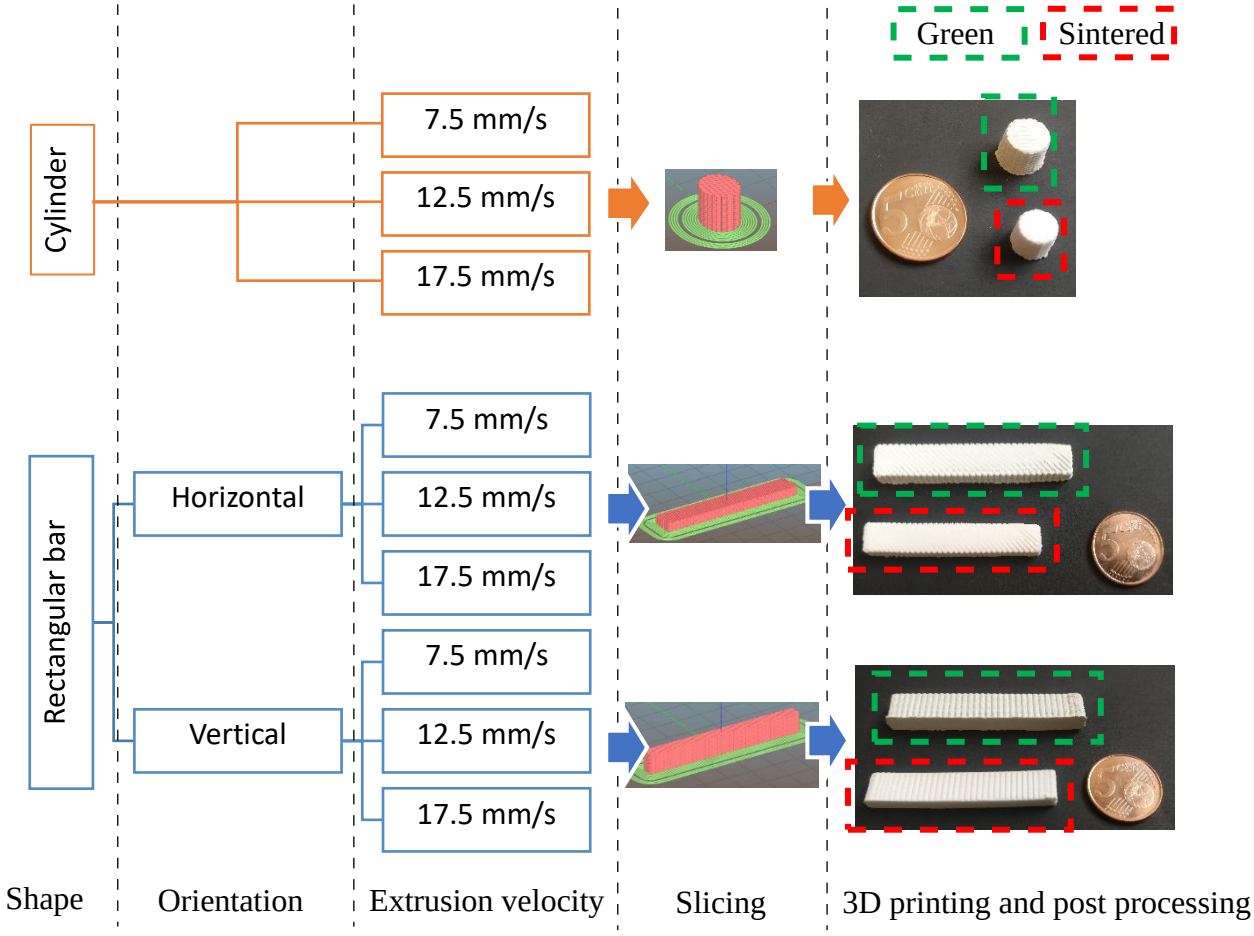

Figure 2: Experimental plan for 3D printing of feedstock: shape, orientation and extrusion velocity combinations

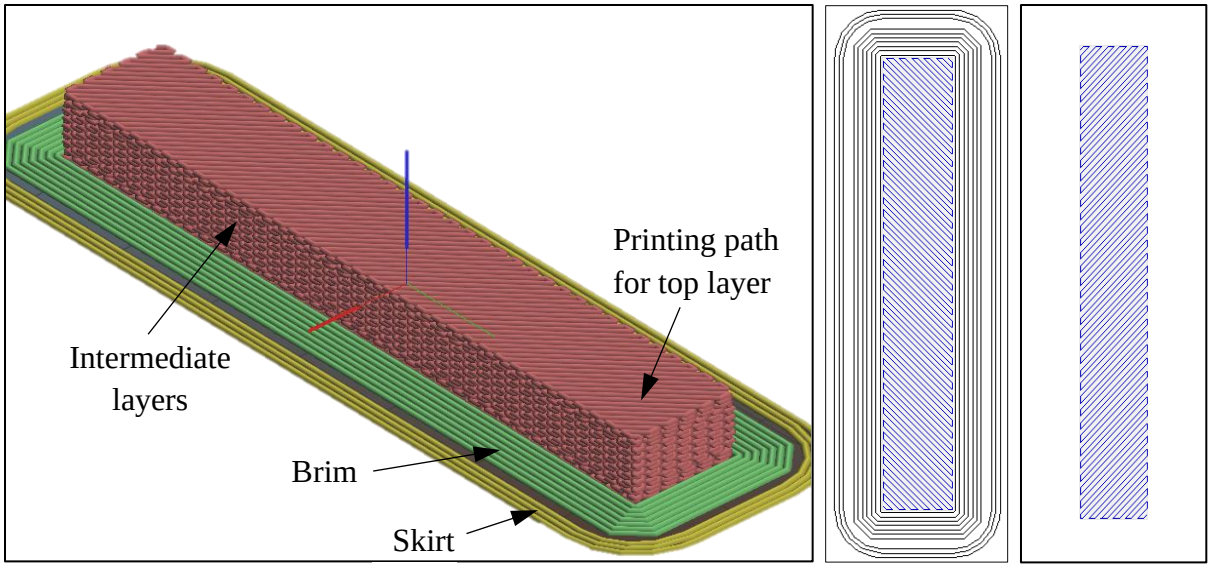

Figure 3: Slicing of part in Slic3r: (a) Elements of sliced horizontal rectangular bar shaped part, (b) printing path for first layer and (c) printing path for second layer

2.3. Post processing of 3D printed parts

Green 3D printed samples were solvent debinded in a bath of agitated water, maintained at 40 ˚C. The tests were performed for 48 hours to ensure maximum removal of sacrificial binder from the feedstock. However, backbone binder was removed by heating the parts in oven without any special atmosphere at a heating rate of 20 ˚C/hr up to a temperature of 145 ˚C with 4 hrs hold time and then at a heating rate of 10 ˚C/hr up to a temperature of 300 ˚C with 2 hrs hold time, followed by natural cooling in oven. The final sintering stage took place in air atmosphere at a temperature of 1620 °C for 1 hr for alumina and 1400°C for 1 hr for zirconia. The increase to the sintering temperature was at a rate of 130 ˚C/hr up to a temperature of 1500 ˚C and then at a rate of 40 ˚C/hr up to 1620 ˚C for alumina parts. Whereas for zirconia parts, the increase to the sintering temperature was at a rate of 100 ˚C/hr up to a temperature of 1250 ˚C and then at a rate of 40 ˚C/hr up to 1400 ˚C. During thermal debinding and sintering, the parts were placed on an alumina plate for ease of handling.

2.4. Characterization of 3D printed and sintered parts

Between the wide ranges of physical and mechanical properties of ceramic parts, in this study, properties were evaluated through the weight change, density, Vickers hardness, flexural strength and fracture toughness measurements on the sintered parts.

The weight of the part through each step of the production process (green, solvent debinded, thermal debinded and sintered) was measured. Three readings per measurement were taken and the average was noted. Sintered density of the parts was measured using Archimedes densimeter by following MPIF 42 standard procedure.

All samples were then polished to have a smooth surface finish because the surface of as printed and as sintered parts is rough due to the chosen printing strategy (without perimeter). In addition to orientation and Ve, hardness was tested by considering face of the rectangular shaped sample as an additional parameter with three levels: top, bottom and side. The hardness of the parts was measured using a micro hardness tester (FM-810, make: Future Tech) at 2 kgf with dwell time of 15 sec. Top and bottom face of horizontal part orientation was designated as L_H x w_H and the side face of horizontal part orientation was designated as L_H x t_H (Figure 4). Similarly, the top and bottom face vertical part orientation was designated as L_V x w_V and the side face of vertical orientation was designated as L_V x t_V. Where $L_H = L_v = 60$ mm, $w_H = t_V = 10$ mm and $t_H = w_V = 6$ mm.

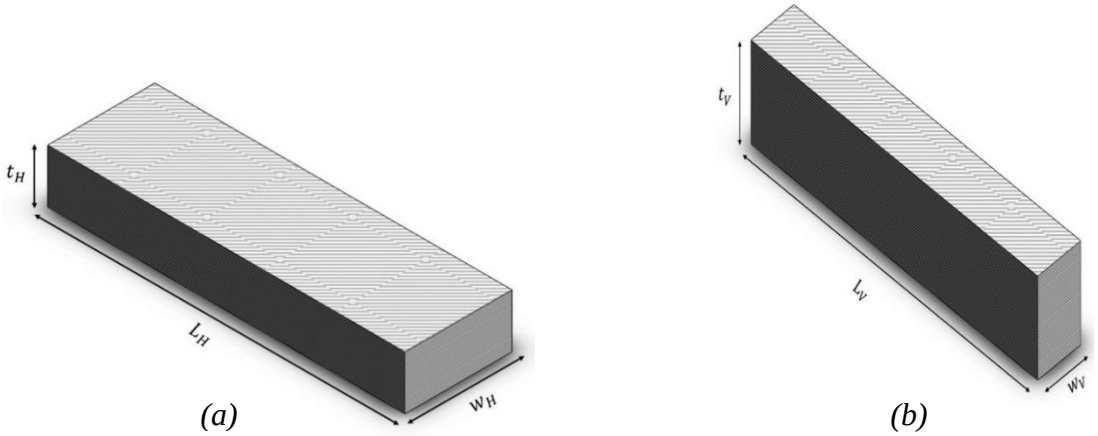

(a) *(b)*

Figure 4: Designation of printing orientations and faces (a) horizontal part orientation and (b) vertical part orientation

The flexural strength was calculated by performing three-point bending tests on rectangular bar shaped parts. ASTM C1674-16 and ASTM A370-18 standards were followed. Bending test was performed on MTS RT/150 machine. Simultaneous crosshead position (mm) were measured by acquiring deflections (mm) using high accuracy deflectometer. All the tests were performed at room temperature under displacement control with a constant crosshead speed of 0.5 mm/min. The loading direction for both configurations was applied on the top face. The span length was set at 30 mm.

The reported values of sintered density, flexural strength are the average of six and three measurements taken from the sintered test specimens, respectively. Also, hardness values reported here is the average of five measurements taken from each side of sintered rectangular bar shaped parts.

The fracture toughness of the sintered part was calculated using the indentation fracture test [28]. In this test a polished sample is indented with a Vickers hardness indenter and the length of the corresponding median cracks is measured. The fracture toughness is related to the indentation load, the size of the median crack, the elastic modulus, and hardness of the material. Six cylindrical samples of each ceramic material were selected for this purpose. They were fine polished using 3-µm diamond suspension and indented at specific marked locations using micro hardness tester (FM-810, make: Future Tech). Micro crack lengths were not visible through micro hardness tester and hence the measurement was carried out in a scanning electron microscope (Zeiss EVO 50XVP SEM) equipped with a backscattered electron detector (BSE). With a load of 2 kgf, cracks were not initiated in the specimens. A possible solution to view the cracks was to increase the load. For that purpose, Ernst-Automatic Hardness tester was used and samples were indented with 60 kgf. Visible cracks were observed as shown in Figure 10 and crack length was measured. Many methods have been developed to calculate K_{IC}, most of which require the values of Young's modulus for their use in addition to the hardness test results. Equation (3) proposed by Niihara et. al is one of the most frequently used for experimental determination of K_{IC} by identification fracture method [29]. Geometrical effects and other terms were rolled up into the dimensionless calibration constants of 0.039 in order to calculate the fracture toughness K_{IC}.

$$K_{IC} = 0.0309 \times \left(\frac{E}{HV}\right)^{\frac{2}{5}} \times \left(\frac{P}{c^{\frac{3}{2}}}\right) \quad (3)$$

where, K_{IC} = Fracture Toughness (MPa$\sqrt{m}$), E = Elastic Modulus (GPa), HV = Vickers hardness (GPa), P = Indent load (N), c = crack length from the center of the indent to the crack tip (m).

3. Results and discussion

3.1 Weight and volume changes through the EAM process stages

WEIGHT LOSS. The weight of parts throughout the EAM process was measured at green, solvent debinded, thermal debinded and sintered states. The percentage weight loss (ΔW) after solvent debinding, thermal debinding and sintering was calculated with reference to the green weight W_{Green} and presented in Figure 5. After solvent debinding, the removal of water soluble binder constituents was about 6÷7% and the additional 6÷7% weight loss after thermal debinding corresponds to the removal of backbone binder. Moreover, it was noted that residual binder constituents were also removed during sintering. Theoretically, there should be no further weight change in sintering, but most of the parts show an additional approximate 2÷3% weight loss during sintering, which corresponds to the removal of residues of binders and loss of some powder from part during the steps.

The expected weight loss after sintering based on feedstock composition is 15.2% and 15.8% for alumina and zirconia respectively. Figure 5 indicates that a comparable weight was lost after the sintering phase for parts printed with any V_e.

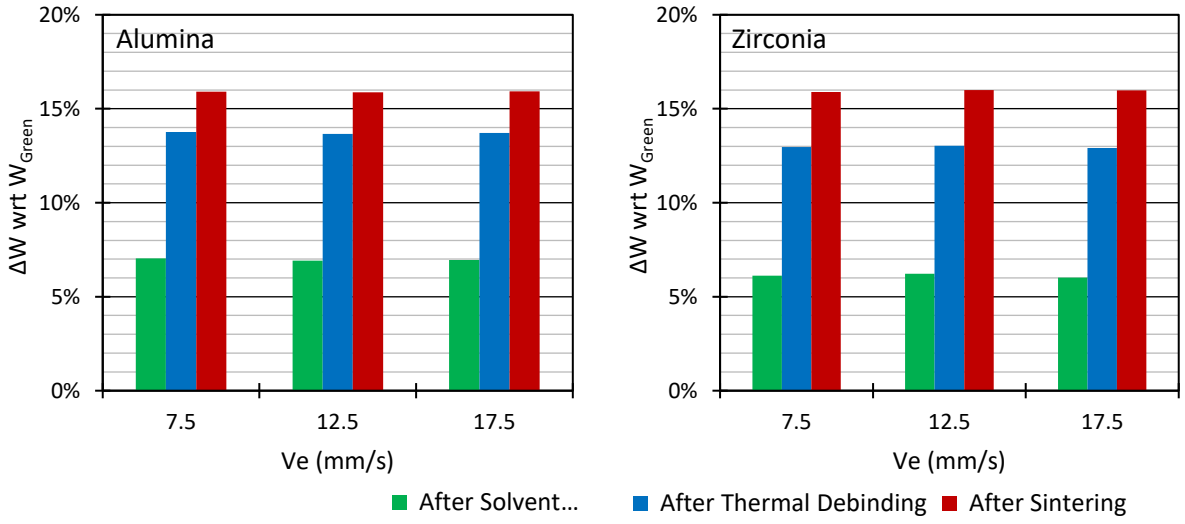

Figure 5: Effect of extrusion velocity on weight loss during EAM process stages

VOLUMETRIC SHRINKAGE. After solvent debinding and thermal debinding, the parts were very fragile. The volume of parts after these steps could not measured; however, visually it appeared a negligible change in total bounding volume and dimensions. On the contrary, sintered parts show significant volume shrinkage caused by densification. The average volumetric sintering shrinkage was calculated through Archimedes principle and shown in Figure 6. Volumetric shrinkage in sintered zirconia parts was found to be ~50%, which was much higher than that of alumina parts ~25%. As a very interesting observation, the volumetric shrinkage significantly varies with part shape and *Ve*. Cylindrical parts show a higher volumetric shrinkage, with respect to rectangular bars, likely because of favorable densification kinetics conditions, due to their lower geometrical volume-to-surface ratio (here).

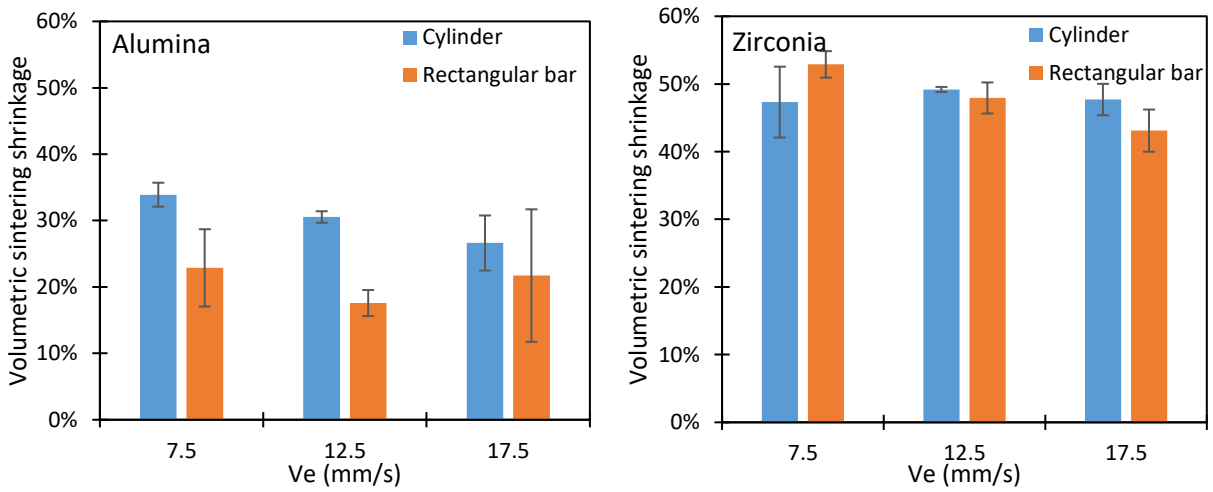

Figure 6: Effect of extrusion velocity on volumetric sintering shrinkage during EAM process

SINTERED DENSITY. Once volume and weight are known, the density can be computed. All parts reached nearly 92% of the theoretical density after sintering. The measured density values ρ are inversely correlated with the extrusion velocity: ρ decreases as *Ve* increases, as shown in Table 3. Unsurprisingly, higher *Ve* values were also found to be inversely correlated to the surface quality of samples. This behavior is not furthered investigated in this paper, because it is well known and typical of all FDM printing processes, where lower extrusion velocity is preferred for improved surface quality by compromising the printing cost and time. The results of Table 3 show that, by

increasing *Ve*, not only the surface quality of parts deteriorates, but also their internal quality, signaled by the density.

Table 3: Theoretical and experimentally determined density ρ (g/cm^3) of sintered ceramics samples

Material	Theoretical/ Feedstock	Experimental for different Ve (mm/s)		
		7.5	12.5	17.5
Alumina	3.95	3.62 ± 0.05	3.60 ± 0.08	3.57 ± 0.03
Zirconia	6.1	5.66 ± 0.00	5.66 ± 0.01	5.64 ± 0.02

3.2 Mechanical properties of sintered parts

The general full factorial experimental analysis was performed for microhardness, the multi-way ANOVA was performed at a 90% confidence interval. The vertical part orientation parts had higher hardness values as compared to horizontal counterparts. Moreover, it is clear from the Figure 7 (a) that within the same orientation, the top face of vertical (L_V x t_V) and the side face of horizontal part orientation (L_H x t_H) respectively had the higher hardness values. This may be because both of these faces have extended load bearing cross section. A similar trend was observed for zirconia specimens. The vertical parts had higher hardness values as compared to horizontal part and within the same orientation.

The stress and strain values were calculated from the three-point bending (load vs. defection) test data using equations 4 and 5.

$$\sigma = \frac{3FL}{2bt^2} \quad \ldots\ldots (4)$$

where σ = instantaneous stress (MPa), F = load (kN), *L* is the span length (distance between center of two supporting pins) (mm), b = width of the specimen (mm), t = thickness of the specimen (mm).

$$\varepsilon = \frac{6t\delta}{L^2} \quad \ldots\ldots (5)$$

where ε = strain, *t* = thickness of the specimen (mm), δ = deflection (mm), *L* = span length (mm).

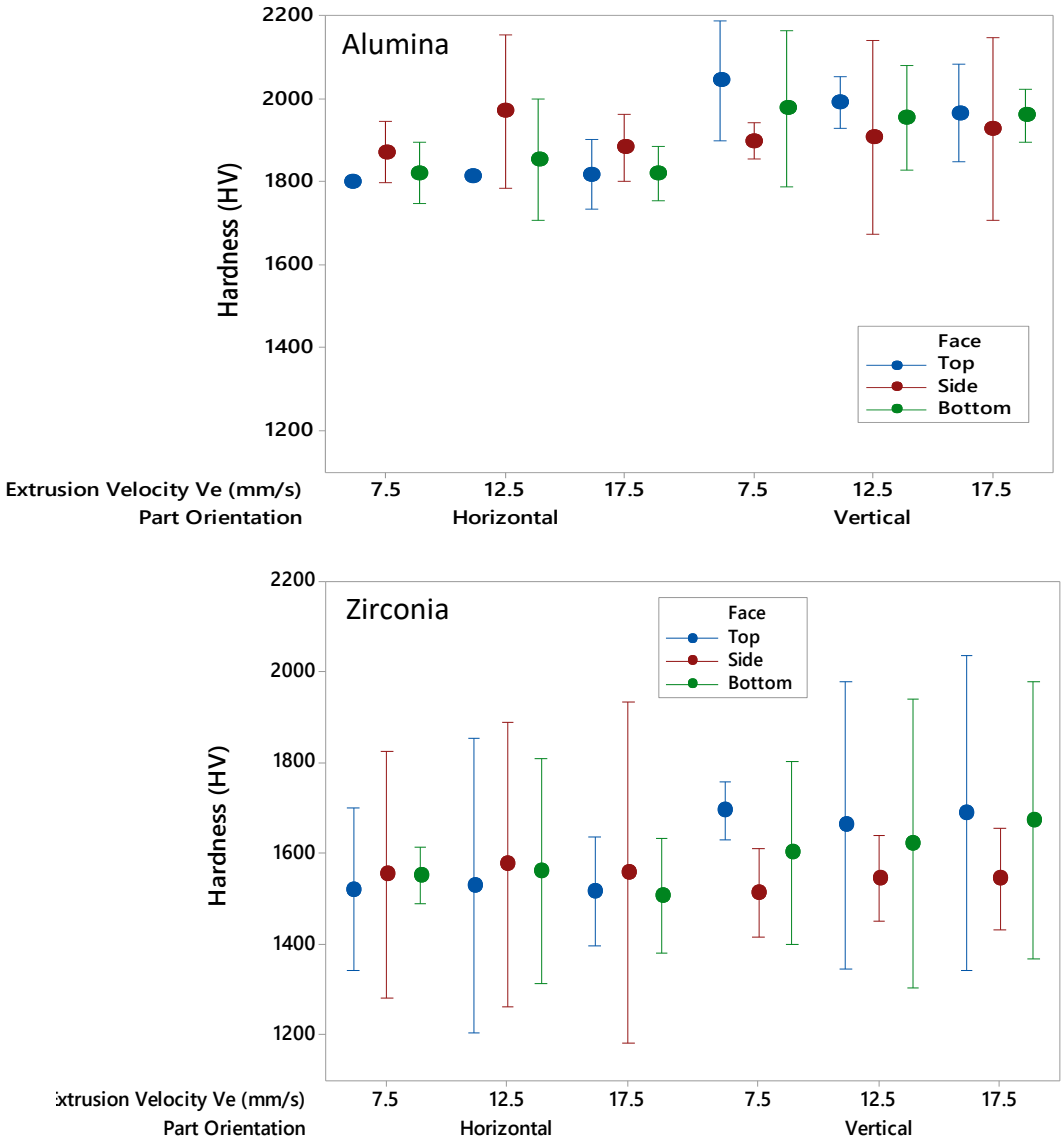

Figure 7: Interval plots for micro hardness of ceramic parts printed with different orientations and Ve

Young's modulus of each specimen was evaluated by approximating the stress-strain curve to a linear regression model until the yield point. The E-value of parts printed with horizontal orientation was higher than vertically printed samples (Fig. 8). This is because during the flexural loading, the crack initiates in the direction of width of the horizontal orientated samples, which was greater than the width of vertical orientation specimens; horizontally printed parts were able to withstand higher load prior to crack and consequently have higher E value.

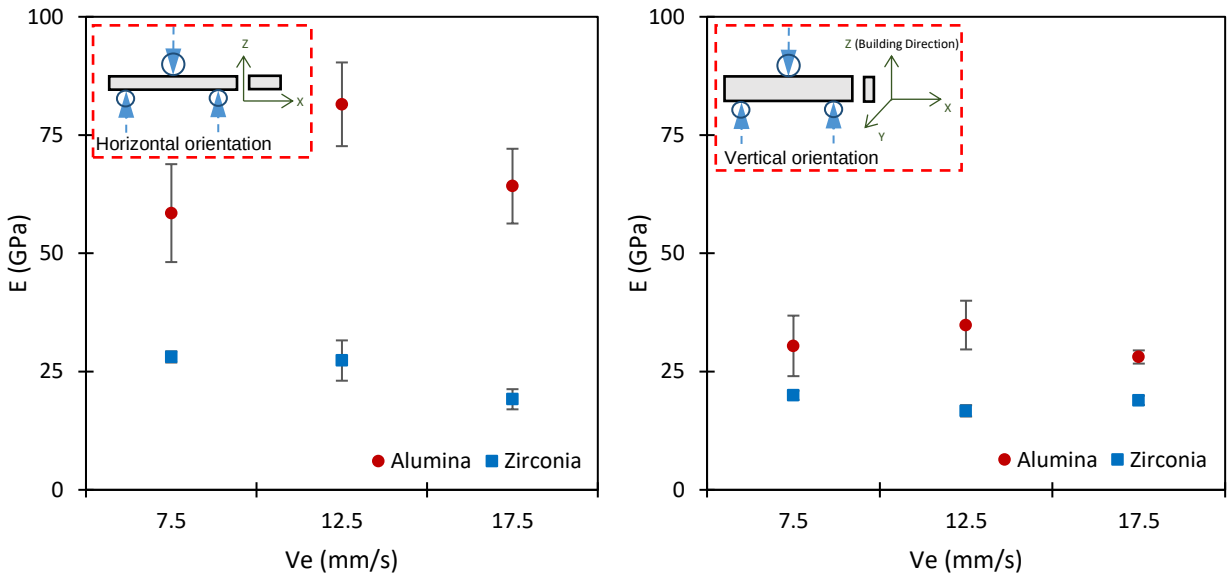

Figure 8: Effect of Ve on elastic modulus (E) of sintered alumina and zirconia parts

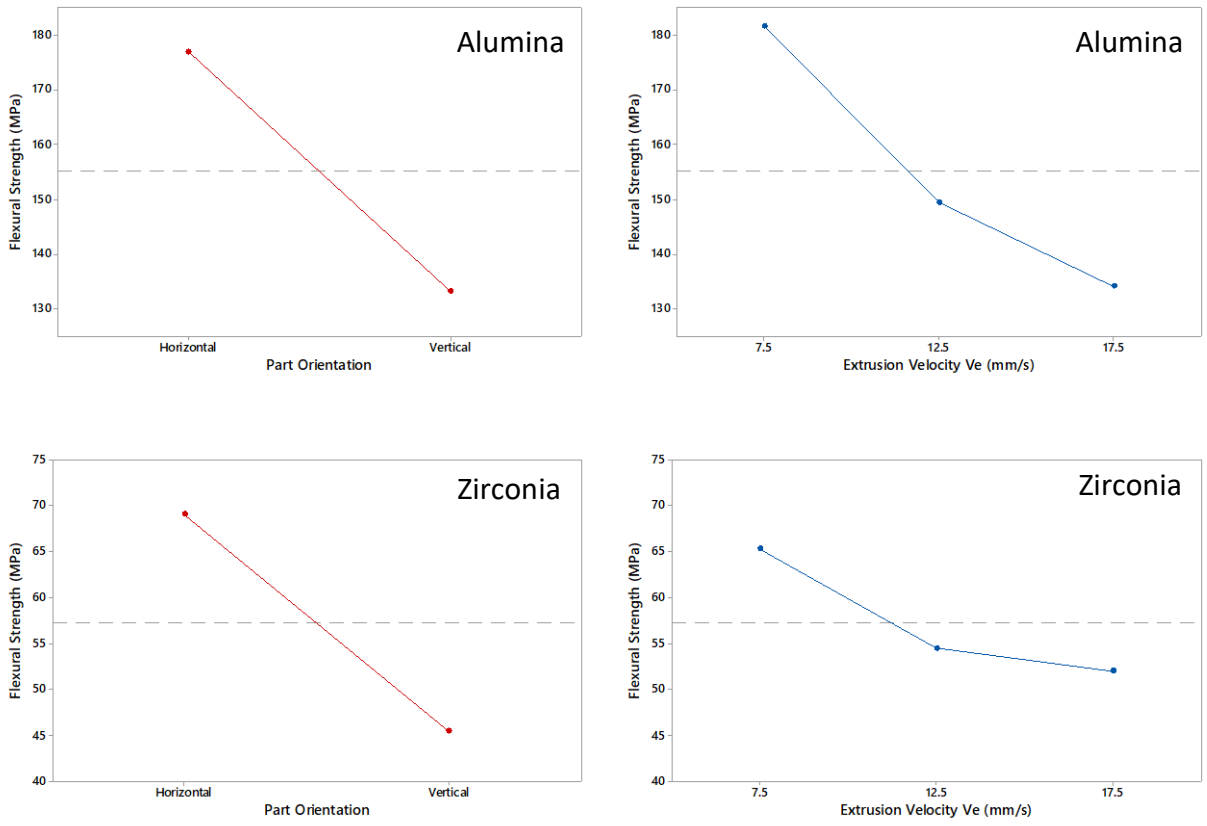

Figure 9: Main effect plots for flexural strength of ceramic parts produced through EAM process

The flexural strength or modulus of rupture was also calculated using equation 3 by substituting the value of maximum load from (load vs. defection) data. The main effects plot for flexural strength is shown in Figure 9. A horizontal line is drawn at the grand mean. The plots depict that the part orientation is affecting the flexural strength significantly whereas for *Ve*, the values of flexural strength are higher for lower speed 7.5 mm/s. A similar trend is observed for both ceramics. The flexural strength of the horizontally printed parts is higher than the vertical ones this is due to the reasons discussed earlier. However, the lower flexural strength of zirconia can be attributed to the existence of random critical flaws present in the samples due to extrusion and deposition issues of zirconia material. There was no complete bonding and fusion between the layers of zirconia specimens and this results in fracture of part within the layers. Alumina, as well as zirconia parts fail by brittle fracture and show almost zero plastic deformation and very low energy absorption at rupture. The fractured zirconia specimens are shown in Figure 10.

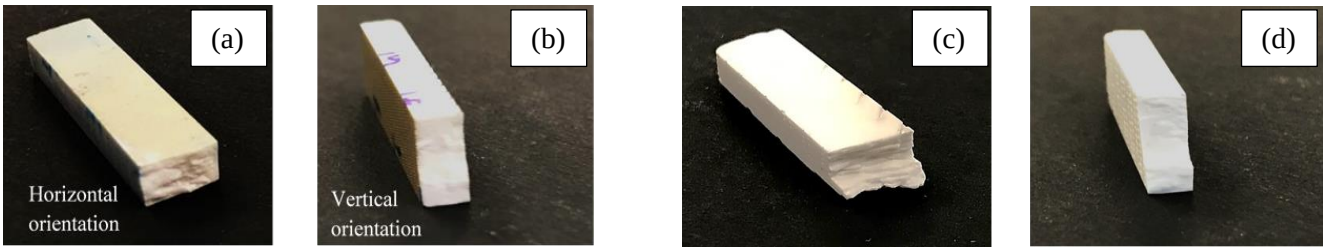

Figure 10: Representative fractured samples of Al_2O_3 printed with (a) horizontal and (b) vertical orientations specimens

The failure of the specimen happens in the thickness direction because crack propagates along the thickness. In the present study, the thickness of parts printed with vertical orientation was higher (and the number of printed layers) than the horizontal parts which allowed these vertical parts to withstand more strains as compared to horizontally printed parts, as a result of which horizontal parts broke at lower strains.

Fracture toughness is determined by indentation fracture method. A hardness test was performed with load of 60 kg to get indentation fracture on the polished surface of cylindrical samples. The values of HV were converted to GPa according to the conversion $\mathrm{HV} \times 0.009807 = 1\ \mathrm{GPa}$. Crack lengths were measured using the direct crack measurement method from SEM images of indented area. The crack length (2c) was measured three times for improving repeatability and the mean

value was computed. Crack-opening profiles showing four cracks arising from Vickers indents are shown in Figure 11; representative measurements for each sample are also marked on the images.

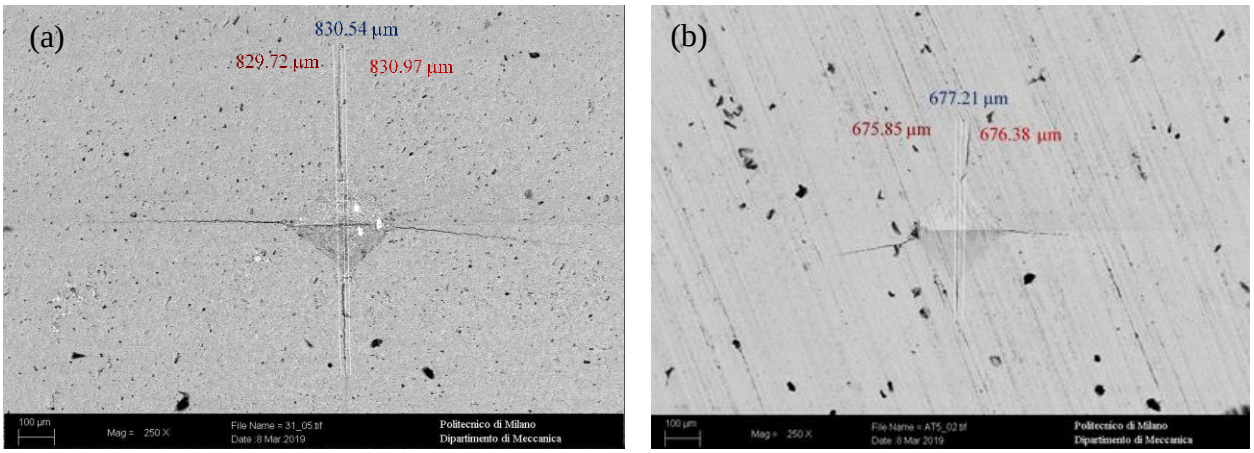

Figure 11: SEM images of (a) alumina and (b) zirconia part showing crack length measurements

Table 4: Fracture toughness K_{IC} ($MPa\sqrt{m}$) of ceramics considered in the present study

Ve (mm/s)	Alumina	Zirconia
7.5	3.5 ± 0.4	3.2 ± 0.8
12.5	3.9 ± 0.2	3.3 ± 0.5
17.5	4.1 ± 0.6	3.5 ± 0.4

K_{IC} shows a marginal increase for both alumina and zirconia with the increase in the extrusion velocity. A possible clarification could be the dependence of K_{IC} on HV and *E*. They both had somewhat neutralized the effect of *Ve* on the K_{IC}. Although indentation fracture method has few drawbacks as there is no universally accepted equation, because different materials have dramatically different deformation and cracking characteristics [30], the values obtained from equation (3) are comparable with reported values of K_{IC} for sintered ceramics studied elsewhere [31].

The correlations of K_{IC} with *E*, *HV*, strain at fracture (ε_f) and flexural strength (σ_f) were observed for both ceramics and are shown in Figure 12. Fracture toughness K_{IC} shows increasing trend with the considered properties of 3D printed ceramic parts and validates the equation (3) proposed by Niihara et. al for conventionally manufactured ceramics.

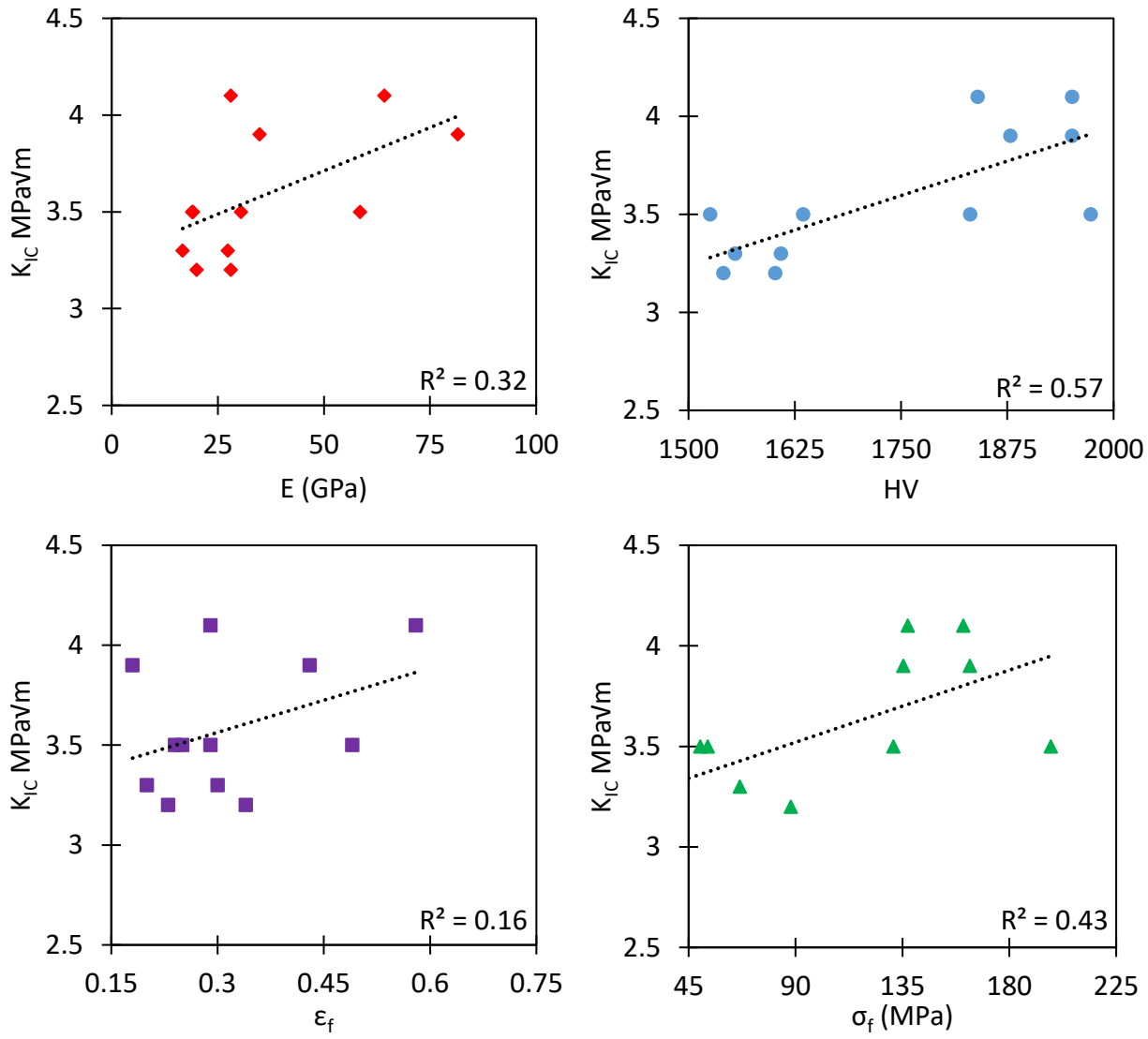

Figure 12: Correlations between K_{IC} and other mechanical properties of 3D printed ceramics parts

4. Conclusion

This study reports the effect of printing process parameters on physical and mechanical properties of extrusion-based additively manufactured ceramic parts. Two ceramic materials alumina and zirconia were considered for this study. The sintered density of ceramic parts was found to be about 8% lower than their respective theoretical density. This is because of lower sintering shrinkage and deposited ceramic structure. The weight change increased with the progression of the debinding and sintering processes due to the removal of binders. Percentage weight change

after solvent debinding and thermal debinding were less for zirconia as compared to alumina even though the binder content was higher in zirconia.

Part orientation was the most significant factor for Vickers hardness in both the ceramic (alumina and zirconia) samples, with vertical orientation specimens showing higher values as compared to a horizontal orientation. Because the load bearing length or resistance to micro-scale penetration (hardness) is higher in the vertical orientation specimens. The extrusion velocity had no clear pattern for both ceramic parts.

The flexural strength of the samples built in horizontal orientation was found to be higher than those of vertical orientation. The crack initiates along the width and horizontal orientation specimens had higher width as compared to vertical ones, due to which the horizontal orientation specimens showed more resistance to crack initiation as a result of which they were able to bear more load and consequently had higher flexural strength values. No clear trend was observed for extrusion velocity.

Fracture toughness of ceramic parts (alumina and zirconia) showed a marginal increase in K_{Ic} with the increase in the extrusion velocity. The correlations of fracture toughness with elastic modulus, hardness, flexural strength, and density were studied. The fracture toughness of both alumina and zirconia showed an increasing trend with the properties considered in equation (3) proposed by Niihara et. al.

References

[1] Barsoum M. Fundamentals of Ceramics. CRC Press; 2019.

[2] Piconi C, Maccauro G. Zirconia as a ceramic biomaterial. Biomaterials 1999;20:1–25. https://doi.org/10.1016/S0142-9612(98)00010-6.

[3] Richerson DW. Modern Ceramic Engineering: Properties, Processing, and Use in Design. CRC Press; 2005.

[4] Kong LB, Huang YZ, Que WX, Zhang TS, Li S, Zhang J, et al. Transparent Ceramics. Cham: Springer International Publishing; 2015. https://doi.org/10.1007/978-3-319-18956-7.

[5] Anstis GR, Chantikul P, Lawn BR, Marshall DB. A Critical Evaluation of Indentation Techniques for Measuring Fracture Toughness: I, Direct Crack Measurements. J Am Ceram Soc 1981;64:533–8. https://doi.org/10.1111/j.1151-2916.1981.tb10320.x.

[6] Apholt W, Bindl A, Lüthy H, Mörmann W. Flexural strength of Cerec 2 machined and jointed InCeram-Alumina and InCeram-Zirconia bars. Dent Mater 2001;17:260–7. https://doi.org/10.1016/S0109-5641(00)00080-4.

[7] Belenky A, Rittel D. Static and dynamic flexural strength of 99.5% alumina: Relation to porosity. Mech Mater 2012;48:43–55. https://doi.org/10.1016/j.mechmat.2012.01.006.

[8] Ćorić D, Renjo MM, Ćurković L, Žmak I. Indentation Fracture Toughness of Y-TZP Dental Ceramics. 16th Int. Conf. New Trends Fatigue Fract., Dubrovnik: 2016.

[9] Doremus RH, Shackelford JF, editors. Ceramic and Glass Materials: Structure, Properties and Processing. Ed. Springer Science + Business Media; 2008.

[10] Chen Z, Li Z, Li J, Liu C, Lao C, Fu Y, et al. 3D printing of ceramics: A review. J Eur Ceram Soc 2019;39:661–87. https://doi.org/10.1016/j.jeurceramsoc.2018.11.013.

[11] Bellini A, Shor L, Guceri SI. New developments in fused deposition modeling of ceramics. Rapid Prototyp J 2005;11:214–20. https://doi.org/10.1108/13552540510612901.

[12] Sing SL, Yeong WY, Wiria FE, Tay BY, Zhao Z, Zhao L, et al. Direct selective laser sintering and melting of ceramics: A review. Rapid Prototyp J 2017;23:611–23. https://doi.org/10.1108/RPJ-11-2015-0178.

[13] Deckers J, Vleugels J, Kruth JP. Additive manufacturing of ceramics: A review. J Ceram Sci Technol 2014;5:245–60. https://doi.org/10.4416/JCST2014-00032.

[14] Zocca A, Colombo P, Gomes CM, Günster J. Additive Manufacturing of Ceramics: Issues, Potentialities, and Opportunities. J Am Ceram Soc 2015;98:1983–2001. https://doi.org/10.1111/jace.13700.

[15] Yang L, Miyanaji H. Ceramic Additive Manufacturing: a review of current status and challenges. Proc. 28th Annu. Int. Solid Free. Fabr. Symp., Austin (TX): 2017, p. 652–79.

[16] Ghazanfari A, Li W, Leu MC, Watts JL, Hilmas GE. Additive manufacturing and mechanical characterization of high density fully stabilized zirconia. Ceram Int 2017;43:6082–8. https://doi.org/10.1016/j.ceramint.2017.01.154.

[17] Huang M, Zhang DQ, Liu ZH, Yang J, Duan F, Chua CK, et al. Comparison study of fabrication of ceramic rotor using various manufacturing methods. Ceram Int 2014;40:12493–502. https://doi.org/10.1016/j.ceramint.2014.04.104.

[18] Wilkes J, Hagedorn Y, Meiners W, Wissenbach K. Additive manufacturing of ZrO 2 -Al 2 O 3 ceramic components by selective laser melting. Rapid Prototyp J 2013;19:51–7. https://doi.org/10.1108/13552541311292736.

[19] Polzin C, Günther D, Seitz H. 3D Printing of Porous Al2O3 and SiC ceramics. J Ceram Sci Technol 2015;6:141–6. https://doi.org/10.4416/JCST2015-00013.

[20] Bae C-J, Halloran JW. Integrally Cored Ceramic Mold Fabricated by Ceramic Stereolithography. Int J Appl Ceram Technol 2011;8:1255–62.

https://doi.org/10.1111/j.1744-7402.2010.02568.x.

[21] Zhou M, Liu W, Wu H, Song X, Chen Y, Cheng L, et al. Preparation of a defect-free alumina cutting tool via additive manufacturing based on stereolithography – Optimization of the drying and debinding processes. Ceram Int 2016;42:11598–602. https://doi.org/10.1016/j.ceramint.2016.04.050.

[22] Gonzalez-Gutierrez J, Cano S, Schuschnigg S, Kukla C, Sapkota J, Holzer C. Additive Manufacturing of Metallic and Ceramic Components by the Material Extrusion of Highly-Filled Polymers: A Review and Future Perspectives. Materials (Basel) 2018;11:840. https://doi.org/10.3390/ma11050840.

[23] Rane K, Strano M. A comprehensive review of extrusion-based additive manufacturing processes for rapid production of metallic and ceramic parts. Adv Manuf 2019;7. https://doi.org/10.1007/s40436-019-00253-6.

[24] Meng J, Loh NH, Fu G, Tay BY, Tor SB. Micro powder injection moulding of alumina micro-channel part. J Eur Ceram Soc 2011;31:1049–56. https://doi.org/10.1016/j.jeurceramsoc.2010.11.034.

[25] Strano M, Rane K, Herve G, Tosi A. Determination of process induced dimensional variations of ceramic parts, 3d printed by extrusion of a powder-binder feedstock. Procedia Manuf 2019;34:560–5. https://doi.org/10.1016/j.promfg.2019.06.220.

[26] Cano S, Gonzalez-Gutierrez J, Sapkota J, Spoerk M, Arbeiter F, Schuschnigg S, et al. Additive manufacturing of zirconia parts by fused filament fabrication and solvent debinding: Selection of binder formulation. Addit Manuf 2019;26:117–28. https://doi.org/10.1016/j.addma.2019.01.001.

[27] Rane K, Barriere T, Strano M. Role of elongational viscosity of feedstock in extrusion-based additive manufacturing of powder-binder mixtures. Int J Adv Manuf Technol 2020;107:4389–402. https://doi.org/10.1007/s00170-020-05323-9.

[28] Liang, K.M., Orange, G. & Fantozzi G. Evaluation by indentation of fracture toughness of ceramic materials. J Mater Sci 1990;25:207–14. https://doi.org/10.1007/BF00544209.

[29] Niihara K. A fracture mechanics analysis of indentation-induced Palmqvist crack in ceramics. J Mater Sci Lett 1983;2:221–3.

[30] Niihara K, Morena R, Hasselman DPH. Evaluation of KIc of brittle solids by the indentation method with low crack-to-indent ratios. J Mater Sci Lett 1982;1:13–6. https://doi.org/10.1007/BF00724706.

[31] Ćorić D, Majić Renjo M, Ćurković L. Vickers indentation fracture toughness of Y-TZP dental ceramics. Int J Refract Met Hard Mater 2017;64:14–9. https://doi.org/10.1016/j.ijrmhm.2016.12.016.